Petroleum Science 21 (2024) 3428–3445

Contents lists available at ScienceDirect

Petroleum Science

journal homepage: www.keaipublishing.com/en/journals/petroleum-science

Original Paper

Failure evaluation mechanism of cement sheath sealing integrity under casing eccentricity during multistage fracturing

Yan Xi [a, *], Yu Yao [a], Xue-Li Guo [b], Jun Li [c, d], Yu-Dong Tian [e], Gong-Hui Liu [a]

[a] Beijing University of Technology, Beijing, 100124, China
[b] CNPC Engineering Technology R&D Company Ltd., Beijing, 102200, China
[c] China University of Petroleum-Beijing at Karamay, Karamay, 834000, Xinjiang, China
[d] China University of Petroleum-Beijing, Beijing, 102249, China
[e] CNPC Daqing Drilling Engineering Corporation, Daqing, 163311, Heilongjiang, China

ARTICLE INFO

Article history:
Received 15 August 2023
Received in revised form
27 April 2024
Accepted 27 April 2024
Available online 3 May 2024

Edited by Jia-Jia Fei

Keywords:
Cement sheath
Microannulus
Casing eccentricity
Numerical simulation

ABSTRACT

A microannulus (MA) is the primary reason for sustained casing pressure in multi-stage fractured-shale gas wells. However, the effect of the casing eccentricity on the long horizontal section has not been considered. In this study, a full-scale integrity tester for cement sheaths is adopted to measure the cumulative plastic deformation. Numerical models are applied to evaluate the development of the cumulative plastic deformation and quantify the MA width considering casing centralization and eccentricity in the context of multiple loading and unloading cycles. Subsequently, the influences of the eccentricity distance and angle, cement-sheath mechanical variables, and different well depths on the cumulative sheath plastic deformation and sheath MA development are explored. The research results demonstrate that casing eccentricity significantly increases the cumulative sheath plastic deformation compared with that of the casing-centered condition. Consequently, the risk of sealing integrity failure increases. The accumulated plastic deformation increases when the eccentricity distance increases. In contrast, the initial plastic deformation increases as the eccentricity angle increases. However, the cumulative plastic deformation decreases after a specific loading and unloading cycle count. Affected by the coupled influence of the internal casing pressure and fracturing stages, the width of the MA in the horizontal section increased from the toe to the heel, and the casing eccentricity significantly increased the MA width at each stage, thus increasing the risk of gas channeling. Finally, an engineering case is considered to study the influence of casing eccentricity. The results show that cement slurries that form low and high elastic moduli can be applied to form a cement sheath when the fracturing stage is lower or higher than a specific value, respectively. The results of this study offer theoretical references and engineering support for the integrity control of cement sheath sealing.
© 2024 The Authors. Publishing services by Elsevier B.V. on behalf of KeAi Communications Co. Ltd. This is an open access article under the CC BY-NC-ND license (http://creativecommons.org/licenses/by-nc-nd/4.0/).

1. Introduction

A cement sheath is positioned into an annular gap between a formation and casing, and plays an essential role in providing zonal isolation and blocking fluid from entering the wellbore in the formation throughout a well lifecycle (Goodwin and Crook, 1992; Wang and Dahi Taleghani, 2014; Zeng et al., 2019; Wei et al., 2022; Yan et al., 2023). However, failure of its sealing integrity frequently occurs in the multi-stage hydraulic fracturing process of horizontal shale gas wells. A range of corresponding experimental research and numerical simulation analyses have been performed to demonstrate the failure mechanism for sheath sealing integrity. The research results have shown that failure was mainly attributable to the multiple loadings and unloadings of the internal casing pressure caused by fracturing in different stages (Shadravan et al., 2015; Wang and Dahi Taleghani, 2017; Li et al., 2020; Xi et al., 2022; Han et al., 2023). However, most studies have focused on casing centralization in the horizontal section as a prerequisite for the research process. In practical engineering, the casing in the horizontal section sinks to the bottom of the horizontal section owing to the long horizontal section in shale gas wells and

* Corresponding author.
E-mail address: xiyan@bjut.edu.cn (Y. Xi).

https://doi.org/10.1016/j.petsci.2024.04.013
1995-8226/© 2024 The Authors. Publishing services by Elsevier B.V. on behalf of KeAi Communications Co. Ltd. This is an open access article under the CC BY-NC-ND license (http://creativecommons.org/licenses/by-nc-nd/4.0/).

relatively large self-weight of the casing strings. This results in casing eccentricity during cementing operations. Indoor experiments and engineering practices have proven that the sheath sealing integrity is more likely to fail once the casing becomes eccentric (Obando Palacio et al., 2020; Huang et al., 2022). However, current research in this area is insufficient. Therefore, analyzing the sheath sealing integrity in a casing-eccentricity scenario is vital for preventing and controlling sustained casing pressure problems.

In previous research, indoor experiments and numerical simulation methods have been adopted to explore the causes of cement-sheath sealing-integrity failure with the casing centered, mainly focusing on two aspects: the stress state analysis of the cement sheath (Andrade et al., 2016; Guo et al., 2018; Bu et al., 2020; Deng et al., 2023) and microannulus (MA) generation and development at the casing-cement sheath interface (Carter and Evans, 1964; Chu et al., 2015; Liu et al., 2016; Deng et al., 2021; Yan et al., 2021; Xi et al., 2022). First, researchers established mathematical models for casing/cement sheath/formation using techniques such as theoretical derivation and numerical simulation, calculated the tangential and radial stresses on the cement sheath by considering the coupling between the internal casing pressure, in situ stress, and reservoir temperature, and evaluated whether cracks would appear on the cement sheath with the stress exceeding the set tensile or compressive strength of the cement (Andrade et al., 2016; Arjomand et al., 2018; Jafariesfad et al., 2020; Wang et al., 2021; Li et al., 2023). As indicated in the study performed by Liu et al. (2021), a lower modulus of elasticity is beneficial for reducing the stress borne by the cement sheath and ensuring its safety. Second, previous studies have investigated MA generation and evolution considering the cyclic loading and unloading impacts of the internal casing pressure in hydraulic fracturing (Zeng et al., 2019; Xi et al., 2020, 2022; Meng et al., 2021). Zeng et al. (2019) conducted full-scale wellbore loading and unloading tests and observed that an MA occurred at the casing and cement sheath interface. Xi et al. (2022) reached similar conclusions through numerical simulations and calculated the distribution pattern of an MA along the entire wellbore. However, all of the above studies were based on the premise that the casing was centered in the horizontal section of the shale gas wells during cementing operations, which was inconsistent with the actual engineering situation.

However, casing eccentricity is actually a necessary consideration in practical engineering. In horizontal shale gas wells, the horizontal section often has a length of over 2000 m. Consequently, the casing may cling to the bottom of the borehole under the action of its weight and the buoyancy generated by the completion fluid, leading to apparent casing eccentricity (Xu et al., 2022; Zeng et al., 2022; Gu et al., 2022). Casing eccentricity can significantly influence cement sheath sealing integrity, as indicated by extant indoor experiments and engineering practice results. Schlumberger's engineering practices in multiple regions, such as the North Sea, have shown that casing eccentricity significantly affected sheath sealing integrity, exacerbating the risk of failure owing to the loss of wellbore sealing integrity (Obando Palacio et al., 2020). Huang et al. (2022) subjected a full-size cement sheath to indoor sealing integrity experiments in a cyclic-load scenario and claimed that casing eccentricity could easily result in MA emergence, thereby deteriorating the sheath sealing integrity. Therefore, evaluating the effect of casing eccentricity on the sheath-sealing integrity during multi-stage fracturing is essential.

However, conducting sealing integrity research for cement sheaths in the context of casing eccentricity faces significant challenges, which are mainly reflected in the following three aspects. First, the degradation process at the sheath interface needs to be considered in the process of analyzing and evaluating the cement sheath sealing integrity, requiring a full-scale experimental tester for verification. However, using such experimental devices to reflect the actual underground situation is very difficult, especially the cyclic internal casing pressure loading and unloading during the multi-stage fracturing process. Second, it is imperative to explore the risk of cement sheath sealing integrity failure over the entire horizontal section, and the influence of the long horizontal shale gas well section should be considered. Nevertheless, differences have been noted regarding the internal casing pressure at varous horizontal section locations and fracturing cycle counts (loading and unloading frequencies), which can affect MA generation and evolution. Third, the eccentricity of the casing can be characterized by the eccentricity distance and angle. During the analysis process, it is necessary to specifically explore the influence of the eccentricity distance and angle on the MA formation and evolution to investigate the sensitivity of the influence of eccentricity parameters.

In this study, a full-scale integrity tester for a cement sheath was adopted to measure the accumulated plastic deformation under the condition of casing centralization. Numerical models were established to investigate the accumulated plastic deformation and calculate the MA width, considering casing centralization and eccentricity. Then, the influences of the eccentricity distance and angle, cement sheath mechanical variables, and different well depths on the accumulated sheath plastic deformation and sheath MA development were investigated. Finally, engineering and geological data of an actual shale gas well were applied to explore the distribution of the MA in the horizontal section under casing-centering and eccentricity conditions. In addition, a corresponding method for using composite cement slurry column structures was proposed. The findings of this study can offer theoretical references and engineering support for ensuring the sealing integrity of cement sheaths.

2. Laboratory experiments

Multi-stage fracturing leads to cyclic internal pressure loading and unloading of casings. Consequently, the cement sheath will exhibit significant plastic deformation. There is a persistent increase in the accumulated plastic deformation as the number of loading and unloading cycles increase. In response, several indoor experiments have been conducted and the law of cumulative plastic deformation has been verified (Liu et al., 2016; Xi et al., 2020). Nevertheless, there are still some differences between triaxial mechanic and full-size cement sheath experiments. Therefore, a full-scale cement sheath integrity measurement experiment was conducted to address this issue based on cyclic loading and unloading conditions.

2.1. Experimental equipment and procedures

A full-scale integrity tester for cement sheaths was adopted to measure and analyze cumulative plastic deformation (Chen et al., 2023). The experimental device included wellbore simulation, control, data collection, and gas-channeling measurement systems, as shown in Fig. 1. The wellbore simulation system was comprised of an outer cylinder and casing with thicknesses of 50 and 7.15 mm and inner diameters of 163.70 and 135.40 mm, respectively, with a height of 1000 mm and steel grade of P110. The cement slurry was poured between the outer cylinder and casing for curing, forming a cement sheath with a wall that was 12-mm thick. The outer and inner sheath diameters were 163.70 and 139.70 mm, respectively.

The interior and exterior walls were arranged with sensors to further analyze the plastic deformation of the cement sheath by measuring the plastic strains imposed on the sheath interior and exterior walls, respectively, as displayed in Fig. 1. In addition, an

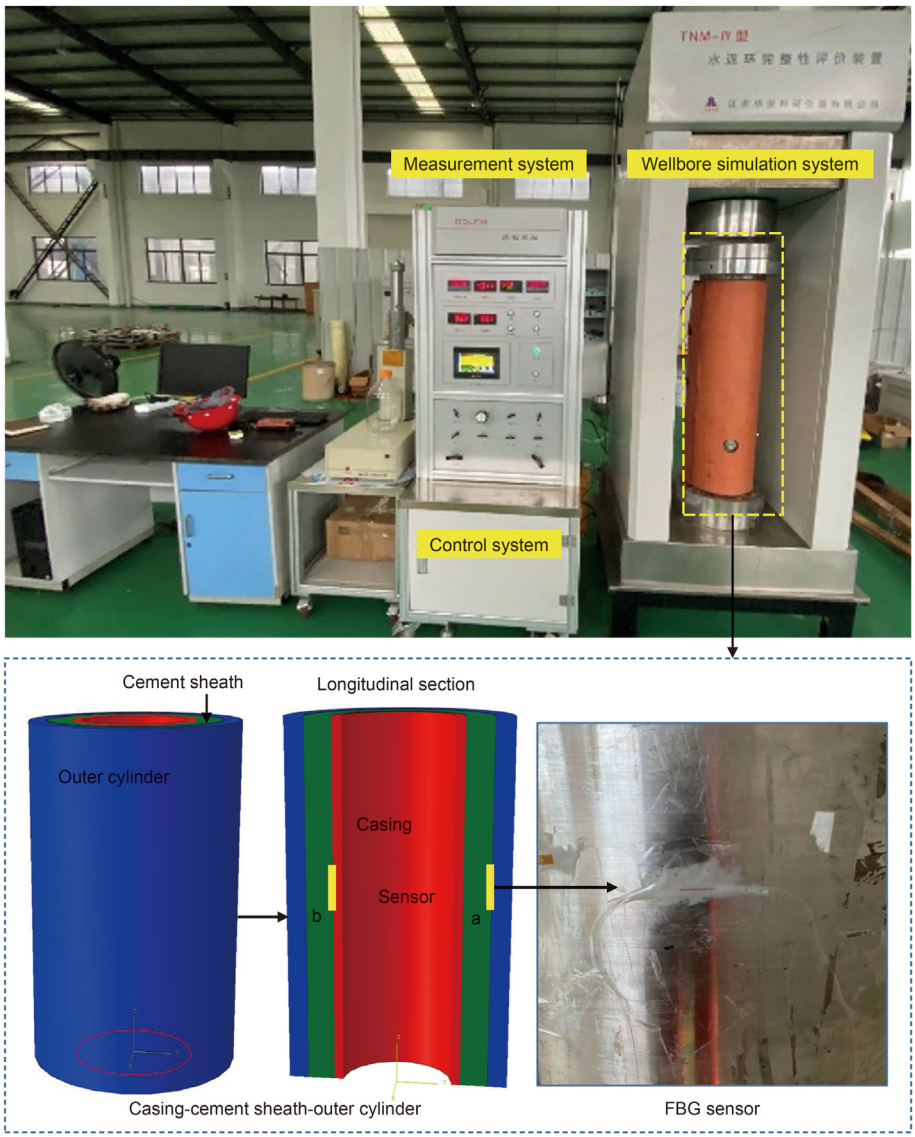

Fig. 1. Full-scale integrity tester for cement sheath.

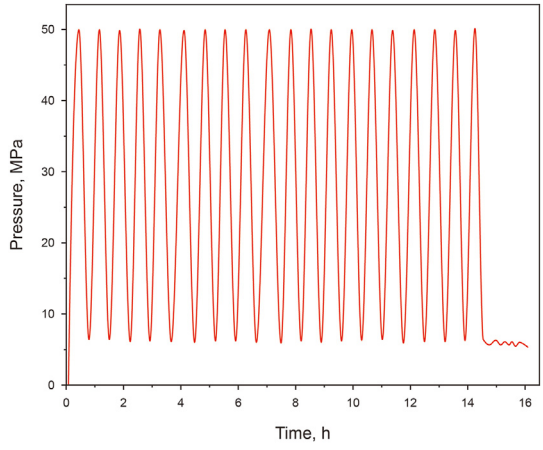

Fig. 2. Upper and lower limits of cyclically loaded and unloaded pressure.

internal pressure was applied to the casing interior wall during the cyclic loading and unloading. The highest and lowest critical pressures were set as 50 and 6 MPa, respectively, as shown in Fig. 2.

2.2. Experimental results

The strain generated during cyclic loading and unloading was recorded and the strain variation patterns at the interior and exterior walls of the cement sheath during the loading and unloading cycles are shown in Fig. 3. The deformation after unloading was used to characterize the cumulative plastic deformation.

The post-unloading deformation was selected for analysis to further quantify and explore the growth pattern of the accumulated plastic deformation, as shown in Fig. 4. Here, an obvious plastic deformation (Phase I) was observed following the first cycle of loading and unloading. The law of plastic deformation growth exhibited a linear variation (Phase II) with an increasing number of cycles.

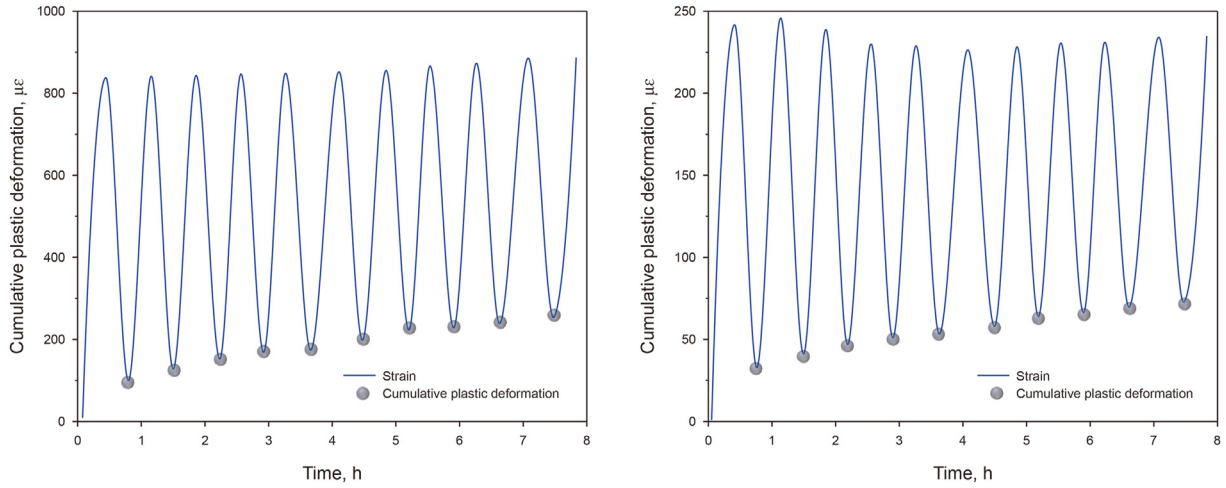

Fig. 3. Accumulated plastic deformations in the course of cyclic loading and unloading.

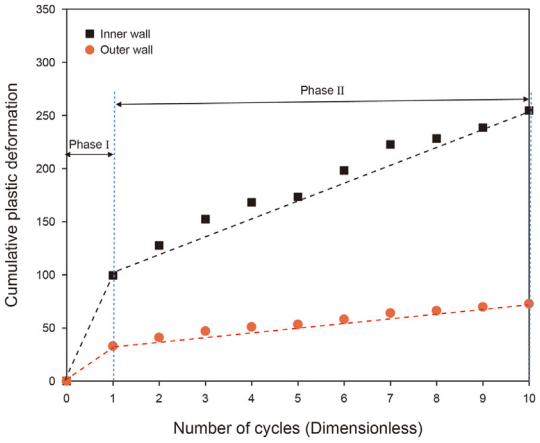

Fig. 4. Deformation under different loading and unloading cycles.

3. Numerical simulations

3.1. Physical and numerical models

Considering that the parameters set by the experimental equipment could not directly reflect the actual underground mechanical environment, it was necessary to establish corresponding numerical models based on the actual geometric dimensions, material parameters, and mechanical environment of a wellbore. Two physical models were considered in this study, as shown in Fig. 5(a) and (b).

The numerical model that was established according to the experimental setup is shown in Fig. 5(a). The geometric dimensions, material parameters, and loading and unloading conditions of the physical model were considered in the establishment process.

The numerical model that was established based on the combination of casing-cement sheath-formation in engineering practice is shown in Fig. 5(b). The casing centralization and eccentricity conditions were considered during the model establishment process, and the casing eccentricity was mainly quantified by the eccentricity distance and angle. All the models were primarily used to calculate the accumulated plastic deformation of the cement sheath in the context of cyclic loading and unloading at different positions on the horizontal section.

The horizontal section is often segmented into 20 stages or more when calculating the horizontal section of an actual well, and the depth of each stage is different. There was also a significant difference in the casing internal pressure of the research object at each stage considering the high frictional resistance of casing fracturing. The calculation method for the internal pressure is expressed as:

$$P_{\text{in}} = P_{\text{wellhead}} + \rho gh - f(l) \tag{1}$$

$$f(l) = \delta l \tag{2}$$

where P_{in} indicates the casing inner pressure (MPa), P_{wellhead} indicates the fracturing pressure (MPa), ρgh denotes the hydrostatic fluid column pressure of the intra-wellbore fracturing fluid (MPa), δ denotes the friction coefficient (MPa/m), and l represents the well depth (m).

3.2. Material parameters and boundary conditions

Regarding the experimental setup-based numerical model, the elastic modulus was 210 GPa for the outer cylinder and casing, and 6.5 GPa for the cement sheath. The Poisson's coefficient setting was 0.21. In terms of input load, the internal casing pressure loading curve during the test process was used as the input parameter to ensure consistency during cyclic loading and unloading.

All parameters in the numerical model for the horizontal section were obtained from actual engineering wells in Luzhou, Sichuan Basin, China. The geometric and material indicators were consistent with those of actual engineering, as listed in Table 1. The casing was made of P110 steel with a yield strength of 758 MPa.

Based on the geological data, the horizontal principal stress ranged from 90 to 110 MPa, whereas the vertical principal stress was 100 MPa. The in situ stress was used for the casing-cement sheath-formation assembly during the numerical simulation process using the predefined field function method.

The treating pressure at the wellhead was 69 MPa and the fracturing fluid had a density and displacement of 1.05 g/cm^3 and 12 m^3/min, respectively. The frictional resistance along the casing during fracturing was 0.0058 MPa/m, as obtained from onsite engineering measurement data. Based on these data, the internal casing pressure could be computed at any position in the horizontal section during the fracturing process and intervals.

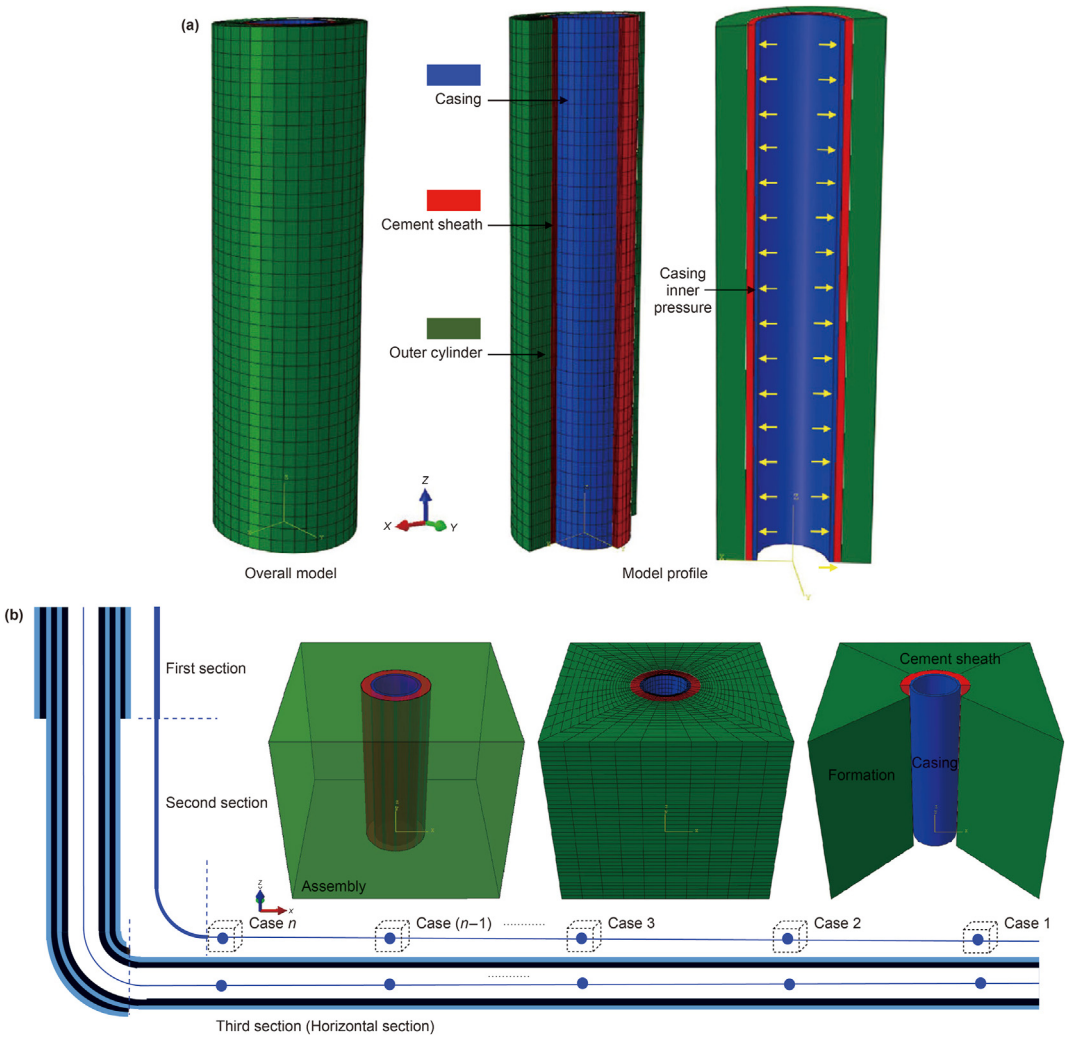

Fig. 5. Numerical models for: (**a**) the experimental device and (**b**) the casing-cement sheath-formation assembly.

Table 1
Geometric and material indicators for casing-cement sheath-formation.

Name	Inner diameter, mm	Elastic modulus, GPa	Poisson's coefficient
Wellbore (formation)	215.9	27	0.22
Cement sheath	139.7	5.5	0.17
Casing	121.36	206	0.3

The cyclic internal loading and unloading pressure in the casing resulted in cumulative plastic deformation at the cement sheath interface during the numerical simulation. The casing-sheath interface was set as a cohesive element to simulate the cumulative plastic deformation generated after each unloading. In addition, the interface followed the traction-separation law, which directly reflected the process of MA emergence and evolution.

The model establishment process was based on prior findings considering the difficulty in obtaining cohesive mechanical parameters (Carter and Evans, 1964; Benzeggagh and Kenane, 1996; Wang and Dahi Taleghani, 2014). Additionally, the relevant parameters were obtained from mechanical experiments, as listed in Table 2. When the yield strength is exceeded, the cement stone begins to enter the plastic range.

3.3. Failure criteria

The cohesive model of the traction-separation law includes cohesive elements and surface interactions, as shown in Fig. 6.

The constitutive model used by the traction-separation law was the bilinear constitutive model displayed in Fig. 6. In addition to describing the linear elastic phase before the material strength reaches the limit value, it represents the linear stiffness decline and softening stage after the limit value has been reached (Feng et al., 2017; Lian et al., 2020). The slope of the linear elastic phase represents the stiffness, and the area under the triangle represents the energy discharge during the fracture process of the material. Hence, the ultimate strength, stiffness, and critical energy discharge were determined based on the cohesion model (or the displacement at failure).

Table 2
Interface bonding indices for the cohesive elements.

Name	Normal stiffness, MPa	Shear stiffness, MPa	Critical energy, J/m^2	Cohesive strength, MPa	Yield strength, MPa
Interface	4.5	0.2	100	8.5	79

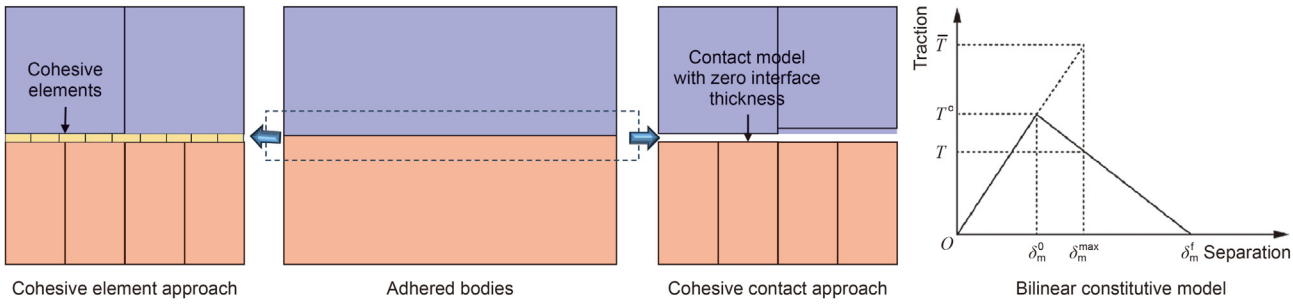

Fig. 6. Cohesive force and bilinear constitutive model.

The early stage of linear elastic traction separation in the entire bilinear structural model is represented as an elastic constitutive matrix, which is expressed as:

$$\begin{Bmatrix} T_n \\ T_s \\ T_t \end{Bmatrix} = \begin{bmatrix} K_{nn} & K_{ns} & K_{nt} \\ K_{sn} & K_{ss} & K_{st} \\ K_{tn} & K_{ts} & K_{tt} \end{bmatrix} \begin{Bmatrix} \delta_n \\ \delta_s \\ \delta_t \end{Bmatrix} \tag{2b}$$

where T_i $(i = n, s, t)$ denotes the nominal vector of traction stress, including one normal and two shear tractions. δ_i $(i = n, s, t)$ represents the nominal vector of separation and K_{ij} $(i, j = n, s, t)$ denotes the stiffness matrix.

The beginning of damage is observed when the value of the interaction function is one, and the contact stress ratio is expressed as:

$$\left\{\frac{\langle T_n\rangle}{T_n^0}\right\}^2 + \left\{\frac{\langle T_s\rangle}{T_s^0}\right\}^2 + \left\{\frac{\langle T_t\rangle}{T_t^0}\right\}^2 = 1 \tag{3}$$

where T_n, T_s, and T_t are the normal, first, and second shear direction tractions at the interface and T_n^0, T_s^0, and T_t^0 indicate their corresponding peak nominal stress values, respectively.

Stiffness degradation can be used for characterizing damage evolution. The scalar damage parameter represents the damage level, which is expressed as:

$$D = \frac{\delta_{\mathrm{m}}^{\mathrm{f}}\left(\delta_{\mathrm{m}}^{\max} - \delta_{\mathrm{m}}^{0}\right)}{\delta_{\mathrm{m}}^{\max}\left(\delta_{\mathrm{m}}^{\mathrm{f}} - \delta_{\mathrm{m}}^{0}\right)} \tag{4}$$

$$\delta_{\mathrm{m}} = \sqrt{\langle\delta_n\rangle^2 + \delta_s^2 + \delta_t^2} \tag{5}$$

where δ_{m} denotes the effective displacement and δ_n, δ_s, and δ_t represent the normal, first, and second shear direction displacements, respectively. δ_{m}^0 and $\delta_{\mathrm{m}}^{\mathrm{f}}$ represent initial damage and complete failure, respectively, and $\delta_{\mathrm{m}}^{\max}$ represents the maximal effective displacement achieved during loading.

Interfacial traction post-damage can be expressed as:

$$T_n = \begin{cases} (1-D)\overline{T_n}, \overline{T_n} \geq 0 \\ \overline{T_n}, \overline{T_n} < 0 \end{cases}$$
$$T_s = (1-D)\overline{T_s} \tag{6}$$
$$T_t = (1-D)\overline{T_t}$$

where $\overline{T_n}$, $\overline{T_s}$, and $\overline{T_t}$ represent optimal elastic tractions in the normal, first, and second shear directions, respectively.

The damage evolution process can be governed using the Benzeggagh-Kenane fracture energy failure mode, which is expressed as:

$$G_n^{\mathrm{c}} + \left(G_s^{\mathrm{c}} - G_t^{\mathrm{c}}\right)\left(\frac{G_s + G_t}{G_n + G_s + G_t}\right)^{\beta} = G_n^{\mathrm{c}} + G_s^{\mathrm{c}} + G_t^{\mathrm{c}} \tag{7}$$

where G_n, G_s, and G_t indicate deformation-induced energy dissipation in the normal, first, and second shear directions, and G_n^{c}, G_s^{c}, and G_t^{c} indicate their individual corresponding critical energies essential for triggering failure, respectively. β denotes a power factor.

3.4. Simulation procedure

The simulation of the numerical model for the experimental device contained two steps. First, the inner surface of the production casing was subjected to an internal pressure. The fluctuation in the internal casing pressure conformed to the loading and unloading laws throughout the experiment. Second, the cement sheath was compressed by the casing under the condition that the internal pressure was loaded and unloaded onto the casing, and the inner surface of the sheath became elastically and plastically deformed because of the radial stress imposed on the inner sheath wall. However, plastic deformation cannot return to its original state after internal pressure unloading; therefore, it contributed to the strain. The cumulative plastic deformation also tended to increase with an increase in the number of loading and unloading cycles.

The simulation of the numerical model for the actual well involved three steps. In the first step, multiple positions in the horizontal section were chosen as research objects, and the

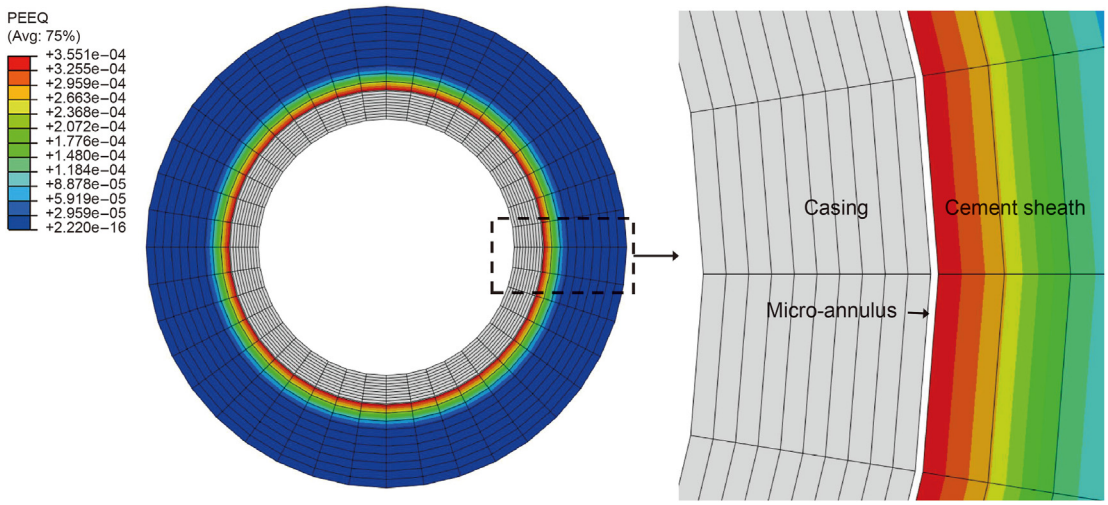

Fig. 7. Cumulative plastic deformation distribution after loading and unloading cycles.

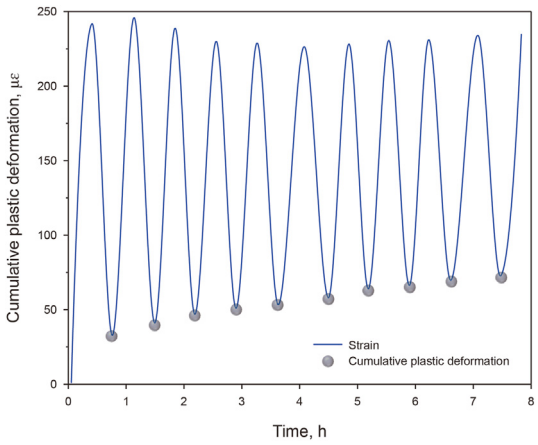

Fig. 8. Alterations in cumulative plastic deformation with the loading and unloading cycle count.

frictional resistance in the fracturing process and internal pressure of the casing at different positions were calculated based on the above formulas. In the second step, the internal pressure of the casing was applied to the inner wall of the casing, and its loading and unloading changes were consistent with those of the engineering construction. In the third step, cumulative plastic deformation developed under the action of three-dimensional geostatic stress (geo-stress), casing internal pressure, and cyclic loading and unloading with a continuous increase in cyclic loading and unloading times, ultimately forming the corresponding MA.

4. Results and discussion

4.1. Verification of numerical simulations

Previous studies have analyzed cumulative plastic deformation using numerical simulations (Xi et al., 2018, 2022). Based on the numerical model established with the experimental parameters, there was significant plastic deformation on the cement sheath

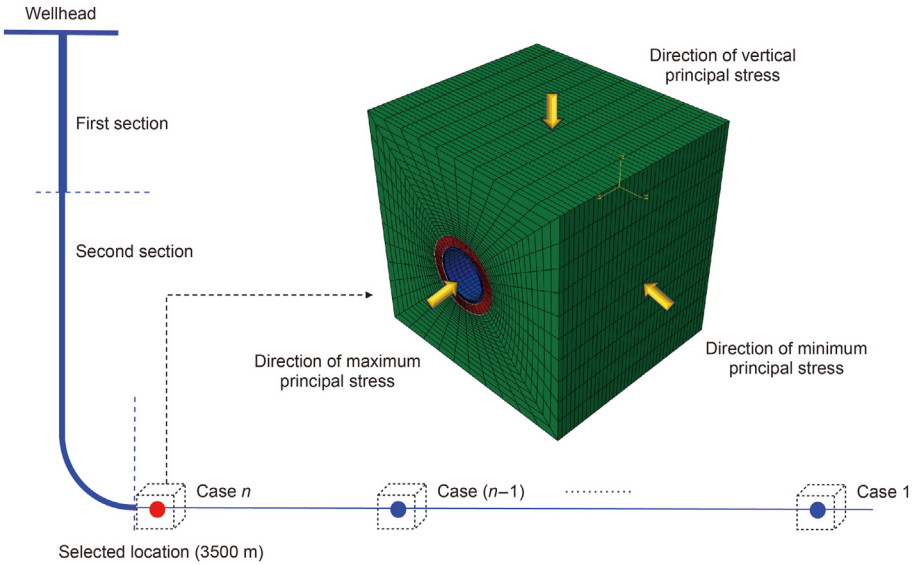

Fig. 9. Selected location and direction of in-situ stress.

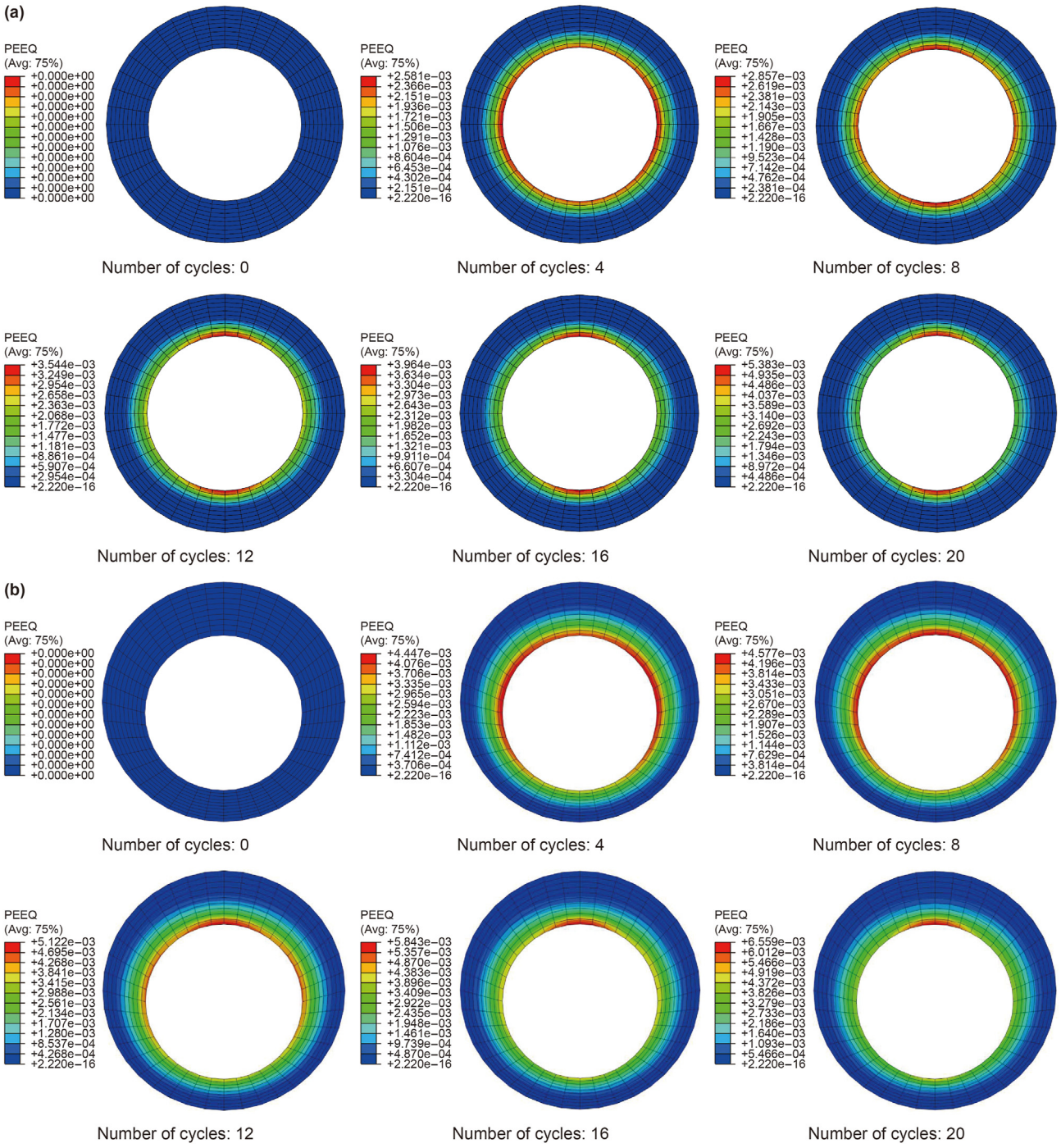

Fig. 10. Accumulated plastic deformations undergone by cement sheath under variation law for: (**a**) casing centering and (**b**) casing eccentricity.

interior wall that led to its separation from the outer wall of the casing, forming an MA for gas channeling (Fig. 7). This was similar to the findings of previous studies and consistent with the experimental results, demonstrating the correctness of this model.

In addition, the plastic deformation of the interior wall of the cement sheath was selected for testing. The variation pattern of the accumulated plastic deformation with increasing loading and unloading cycles was analyzed, as presented in Fig. 8. It is worth noting that the numerical simulations and measurement results were consistent.

4.2. Comparative analysis of casing centering and eccentricity

The casing internal pressure (105.4 MPa) and fracturing stage (20 stages) conditions at a well depth of 3500 m were selected as the basic parameters to compare and study the differences in MA emergence and development under casing centralization and eccentricity scenarios during multi-stage fracturing. The casing eccentricity angle was set to 0° and the eccentricity distance was set to 10 mm. The generation and development processes of the accumulated plastic deformation and MA were calculated and analyzed under casing centering and eccentricity conditions based

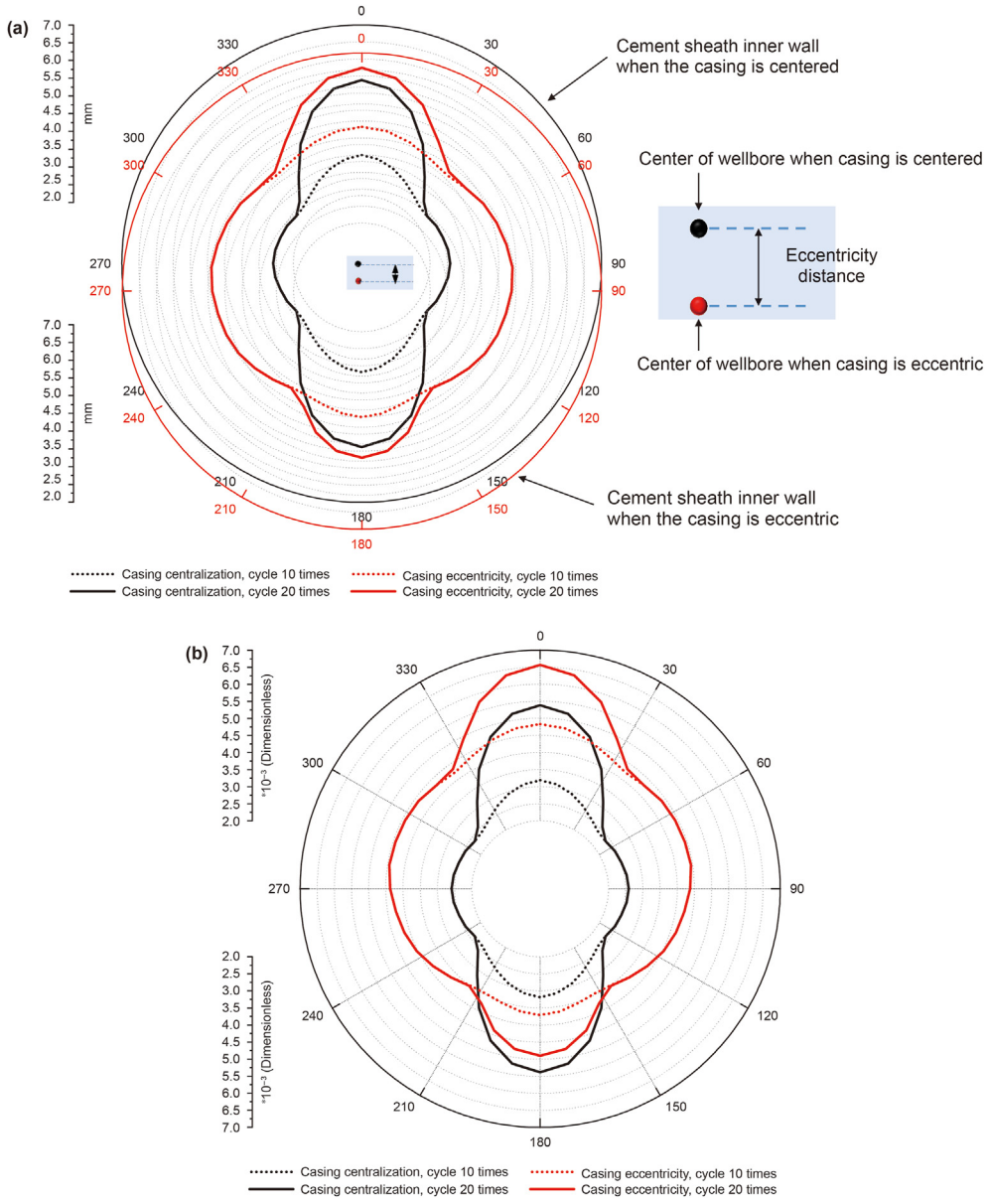

Fig. 11. Changes in cumulative plastic deformation under centered and eccentric casing conditions: (**a**) before and (**b**) after unifying the wellbore center.

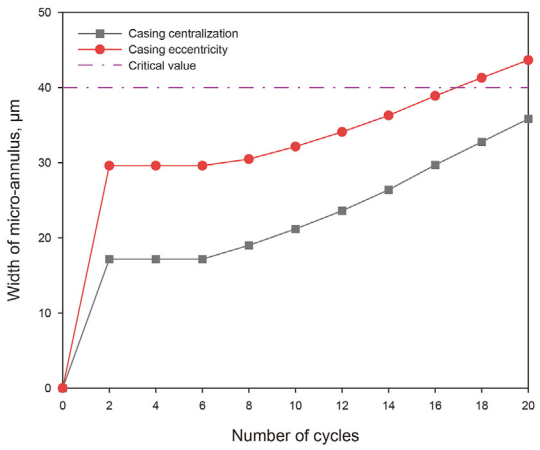

Fig. 12. Variation patterns of MA width and critical value of gas channeling.

on these engineering and geological parameters. The selected location and direction of in-situ stress are shown in Fig. 9.

Previous research has always used the parameter of equivalent plastic strain (PEEQ) to characterize cumulative plastic deformation (Xi et al., 2021). The development law of the PEEQ when the casing was centered and eccentric during multistage fracturing is shown in Fig. 10.

The following observations were made based on this figure.

(a) The loading and unloading cycle counts increased when the casing was centered in the wellbore. Therefore, plastic deformation occurred on the cement sheath interior wall. The position where the maximum plastic deformation first appeared on both sides of the sheath interior wall was parallel to the minimum horizontal principal stress owing to the influences of the vertical and minimum horizontal principal stresses. The position where the maximum plastic deformation occurred changed as the cycle count increased,

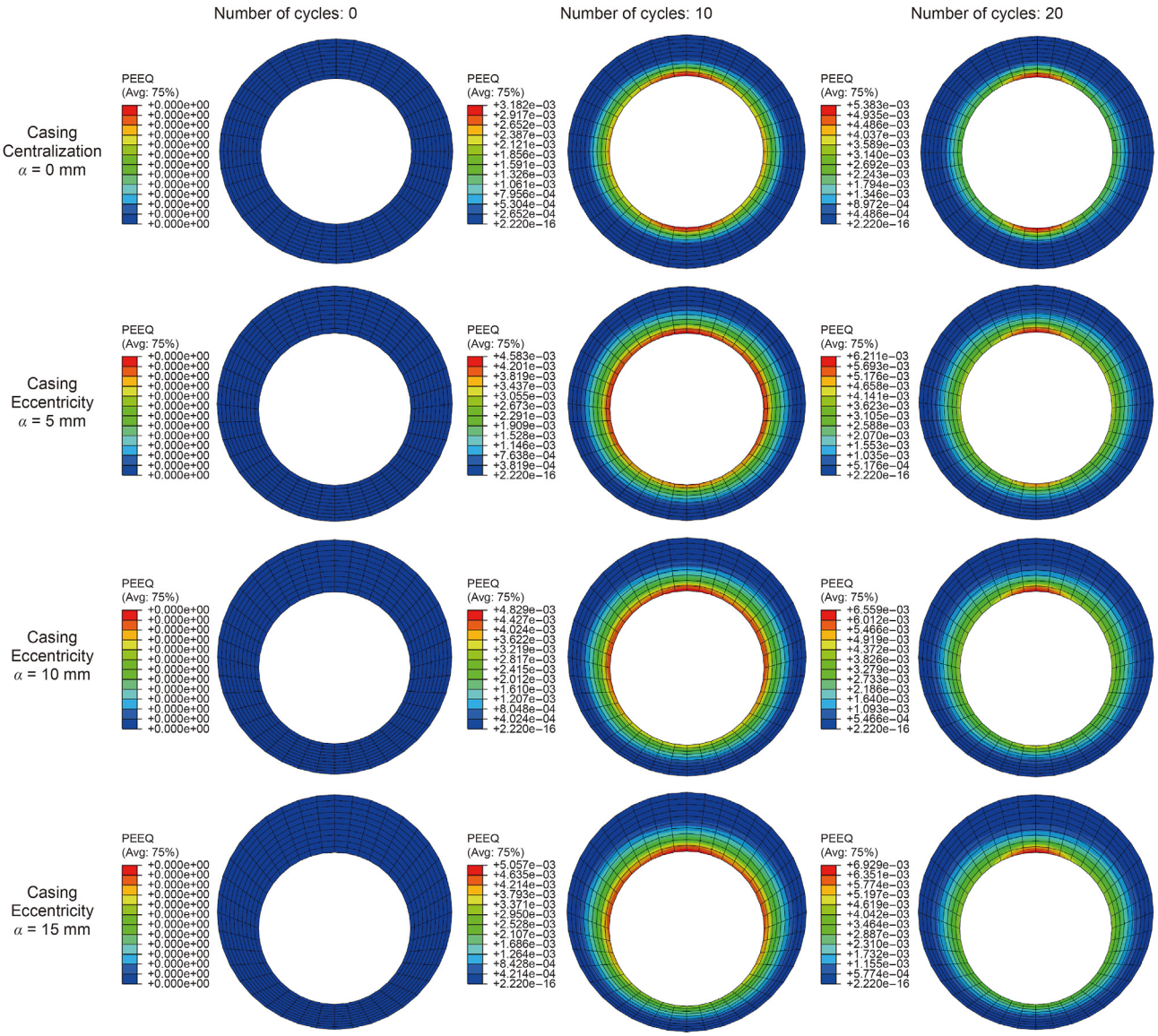

Fig. 13. Cumulative plastic deformation distributions under different eccentricity distances.

appearing in the upper and lower segments of the cement sheath perpendicular to the vertical principle.

(b) Plastic deformation emerged on the inner cement sheath wall when the casing was eccentric as the loading and unloading cycle counts constantly increased, showing persistent development. Plastic deformation occurred primarily on both sides of the inner sheath wall during the early phase of cyclic loading and unloading (cycle counts $\leq$4). The top part of the inner sheath wall became the primary site of plastic deformation with an increase in the number of loading and unloading cycles, which was perpendicular to the vertical ground stress.

(c) The generated cumulative plastic deformation was greater when the casing was eccentric, under the condition that the cycle count for loading was identical to that for unloading. This was determined by comparing the PEEQ values under the casing centralization and eccentricity scenarios. The maximum cumulative plastic deformations for the 4th and 12th cycles under the casing centralization and eccentricity scenarios were 2.58‰ and 3.54‰, and 4.45‰, and 5.12‰, respectively. Under the eccentricity condition, the PEEQ increased by 72.5% and 44.6%, respectively, compared to those of the centralization condition.

The accumulated plastic deformation distributions along the sheath interior wall were compared to further quantify the difference in the cumulative plastic deformations caused by the cement sheath in the casing centralization and eccentricity scenarios after cyclic loading and unloading, as shown in Fig. 11.

The loading and unloading cycle counts were 10 and 20, respectively. The following observations were made based on this figure.

(a) The positions of the wellbore center were different when the casings were centered and eccentric, and the distance between the wellbore centers under both conditions represented the eccentricity distance. The distribution of the accumulated plastic deformation on the sheath interior wall

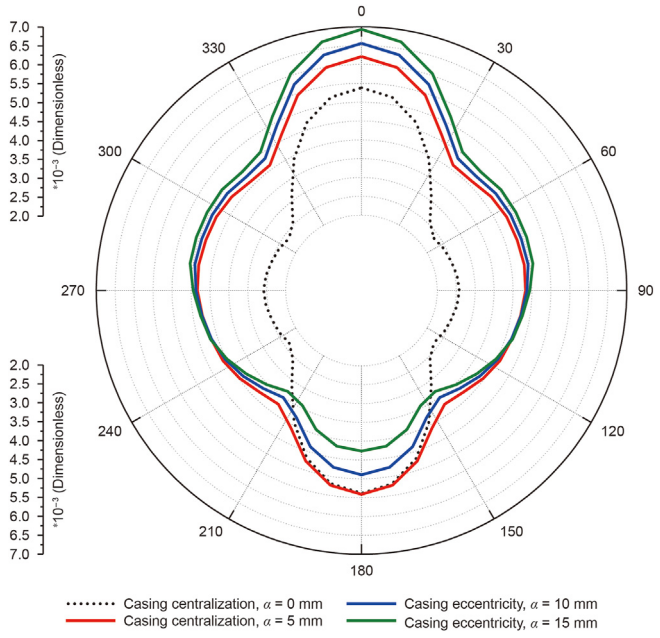

Fig. 14. Development law of cumulative plastic deformation distributions under different eccentricity conditions.

did not significantly change when there was eccentricity in the casing, as shown in Fig. 11(a). This was primarily owing to the significant cumulative plastic deformation occurring at the upper and lower sheath ends. The increase in the cumulative plastic deformation at these ends was more significant with an increase in the cycle count (from the 10th to 20th cycles). The accumulated plastic deformation on both sides scarcely changed.

(b) The wellbore center was normalized to the same position under centered and eccentric casing conditions to further quantify and explore the distribution of cumulative plastic deformation, as shown in Fig. 11(b). When the number of cycles was 10, the accumulated plastic deformations borne by the cement sheath were 3.18‰ and 4.83‰ when the casing was centered and eccentric, respectively. The corresponding cumulative plastic deformations increased to 5.38‰ and 6.56‰ and the growth rates were 69.2% and 35.8%, respectively, with a further increase in the cyclic loading and unloading frequency (20 cycles). Overall, the eccentricity of the casing significantly increased the accumulated plastic deformation of the cement sheath interior wall, increasing the failure risk of the sheath sealing integrity.

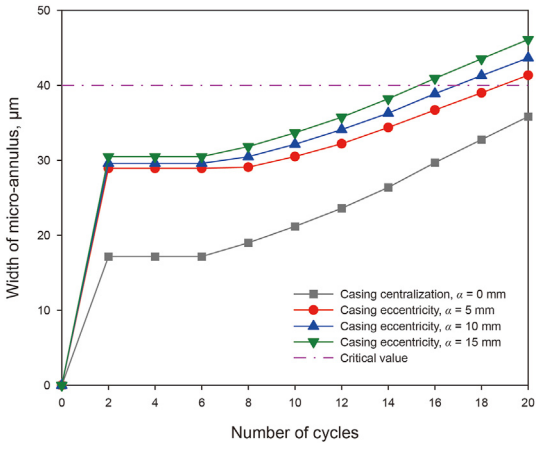

Fig. 15. Generation and development of MA under different eccentricity distances.

The width of the resulting MA was calculated based on the cumulative plastic deformation of the inner wall of the cement sheath (Xi et al., 2021, 2022), as presented in Fig. 12. Here, the variation pattern of the MA width is shown as the number of cycles increases. According to previous research, it is easy to cause gas leakage when the width of the MA is 40 μm (Xi et al., 2021). Therefore, this value was used as the critical value for gas channeling. Under the condition that the number of loading and unloading cycles reached 17, the widths of the MA were 31.2 and 40.1 μm when the casing was centered and eccentric, respectively. The last width exceeded the critical value of gas channeling.

4.3. Sensitivity analysis

4.3.1. Influence of eccentricity distance

The eccentricity distance of the casing was mainly used to characterize the distance between the centers of the casing and wellbore. As previously mentioned, the casing's self-weight was relatively high when the casing in the horizontal section was extended. The casing may experience varying degrees of sinking under the combined action of cement slurry buoyancy and stabilizer support, resulting in different eccentricities. In this case, different eccentricity distances were used to characterize the degree of eccentricity.

The location at a well depth of 3500 m was selected as the analysis object, there were 20 fracturing stages, and the eccentricity angle was set to 0°. The cumulative plastic deformation changes of the cement sheath inner wall and the generation and development of the MA were analyzed at eccentricity distances of 0, 5, 10, and 15 mm.

Cumulative plastic deformations under varying eccentricity distance conditions considering loading and unloading cycles of 0, 10, and 20 are shown in Fig. 13.

The following observations were ascertained based on this figure.

(a) The cumulative plastic deformation tended to increase continuously under the same mechanical environment and cyclic loading and unloading times as the eccentricity distance increased. The cumulative plastic deformations when there was no casing eccentricity were 3.18‰ and 5.38‰ after 10 and 20 loading and unloading cycles, respectively. The cumulative plastic deformations for eccentricity distances of 5 and 15 mm under the same cycling conditions were 4.58‰ and 6.21‰, and 5.06‰ and 6.93‰, respectively. Compared with the casing-centered condition, these were increases of 44.02% and 15.43%, and 59.12% and 28.81%, respectively. This indicated that the eccentricity distance of the casing further exacerbated the risk of cement sheath sealing integrity failure.

(b) The eccentricity distance of the casing changed the distribution of the cumulative plastic deformation on the inner wall of the cement sheath compared to that where the casing was centered. The eccentricity of the casing changed the shape of the cement sheath under the combined action of the minimum horizontal and vertical geo-stresses, affecting the distribution area of the cumulative plastic deformation. The maximum position of the cumulative plastic deformation gradually approached the top of the inner wall of the cement

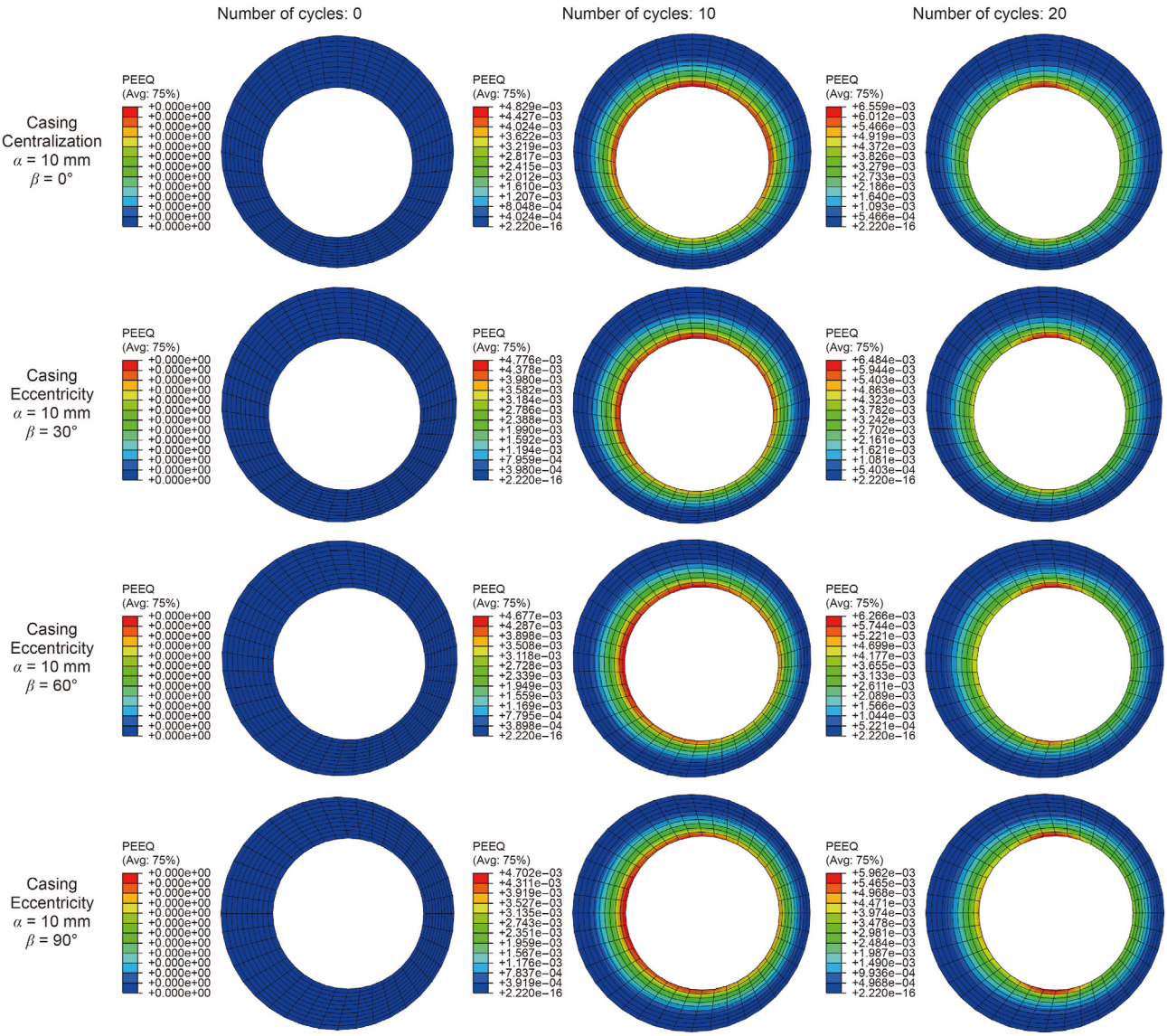

Fig. 16. Cumulative plastic deformation distribution changes under different eccentric angles.

sheath as the eccentricity continued to increase when the number of loading and unloading cycles was 10 and the eccentricities were 5, 10, and 15 mm.

Nodes on the inner wall of the cement sheath were used to extract the cumulative plastic deformation values along the circumference to further analyze the cumulative plastic deformation area and corresponding changes in values under different eccentricity distances. In addition, the casing centers under different eccentricity conditions were subjected to a concentric treatment to express the cumulative plastic deformation more accurately, as shown in Fig. 14.

The risk area of cumulative plastic deformation mainly appeared at the top of the casing when there was casing eccentricity owing to the combined influence of the in situ stress and eccentricity state. The maximum cumulative plastic deformation was 5.38‰ when the casing was centered. The maximum cumulative plastic deformation values were 6.21‰, 6.56‰, and 6.93‰ when the eccentricities were 5, 10, and 15 mm, respectively. The corresponding cumulative plastic deformations for the centered condition increased by 15.4%, 21.9%, and 28.8%, respectively.

The generation and development of MA under different eccentricity distance conditions are shown in Fig. 15.

The following observations were ascertained based on this figure.

(a) The generation and development of the MA exhibited similar variation patterns under centering and eccentricity casing conditions. The initial plastic deformation increased significantly when there was casing eccentricity. In addition, the width of the initial MA increased as the eccentricity distance continued to increase. The width of the MA under casing eccentricity and the same number of loading and unloading cycles was significantly wider than that under the centered-casing condition.

(b) As previously mentioned, gas channeling occurs when the width of an MA reaches 40 μm (Xi et al., 2022). The width of the MA was 35. 8 μm after 20 cycles of loading and unloading when the casing was in the center, and there was no evidence of gas channeling. However, the width of the MA

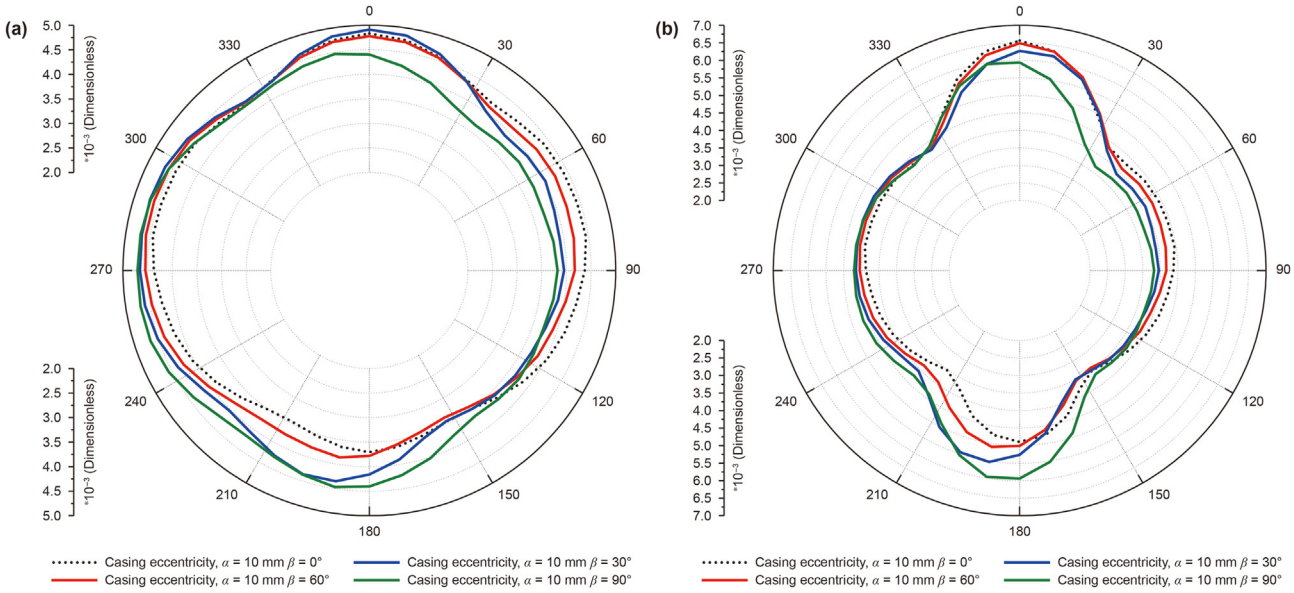

Fig. 17. Changes in cumulative plastic deformation distribution areas under different eccentric angles after: (**a**) 10 and (**b**) 20 loading and unloading cycles.

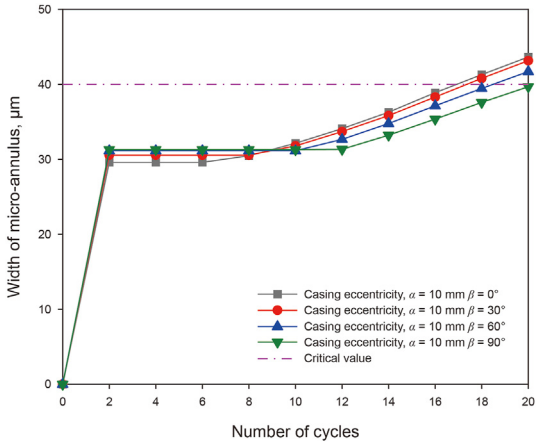

Fig. 18. Generation and development of the MA gap under different eccentricity angles.

exceeded 40 μm (40.2 μm) when the casing underwent eccentricity at a distance of 5 mm for the 19th loading and unloading cycle, causing failure of the sealing integrity at this depth. Similarly, the critical value of gas channeling was exceeded when the eccentricity distances were 10 and 15 mm for the 17th and 16th loading and unloading cycles, respectively. Therefore, the more significant the eccentricity distance, the lower the durability of the cement sheath under the same conditions.

4.3.2. Influence of eccentricity angle

The eccentricity distance was set to 10 mm to further analyze the influence of the eccentricity angle on cumulative plastic deformation. The eccentricity angles were set to 0°, 30°, 60°, and 90°, as shown in Fig. 16.

The existence of an eccentricity angle changed the distribution of the cumulative plastic deformation owing to the impact of nonuniform ground stress. This effect was more significant when the number of loading and unloading cycles was 10. The position of the maximum cumulative plastic deformation changed with the increasing eccentricity angle, as shown in Fig. 16. This situation made the location of the accumulated plastic deformation on the inner wall of the cement sheath more complex, thus increasing the implementation difficulty for later treatment measures. However, the maximum cumulative plastic deformation position remained at the top of the inner wall of the cement sheath when the number of loading and unloading cycles was 20.

The cumulative plastic deformation under different eccentric angles was analyzed to quantify its distribution on the inner wall of the cement sheath, as shown in Fig. 17. The effect of the casing eccentricity angle on the cumulative plastic deformation value was not significant. However, it had a more substantial impact on the cumulative plastic deformation area. The maximum cumulative plastic deformation areas mainly appeared at the top and bottom of the inner wall of the cement sheath and on the left side when the loading and unloading cycles were repeated ten times. However, the maximum cumulative plastic deformation areas mainly appeared at the top and bottom as the number of loading and unloading cycles continued to increase. This affected the sealing integrity of many areas above the cement ring, thereby increasing the difficulty of governance.

The generation and development of the MA at different eccentricity angles were calculated based on the above results, as shown in Fig. 18.

The eccentricity angle exhibited a relatively small degree of influence on the initial plastic deformation. This indicated that the more significant the eccentricity angle, the greater the initial plastic deformation. However, the eccentricity angle increased and the cumulative plastic deformation decreased as the number of loading and unloading cycles increased past 12.

4.3.3. Influence of mechanical properties of the cement sheath

It was previously established that the mechanical properties of set cement included the elastic modulus, Poisson's ratio, internal friction angle, and cohesion, which have an impact on the cumulative plastic deformation during cyclic loading and unloading (Xi et al., 2020). The elastic modulus has the most significant influence. However, previous research did not analyze the influence of the elastic modulus on the cumulative plastic deformation under

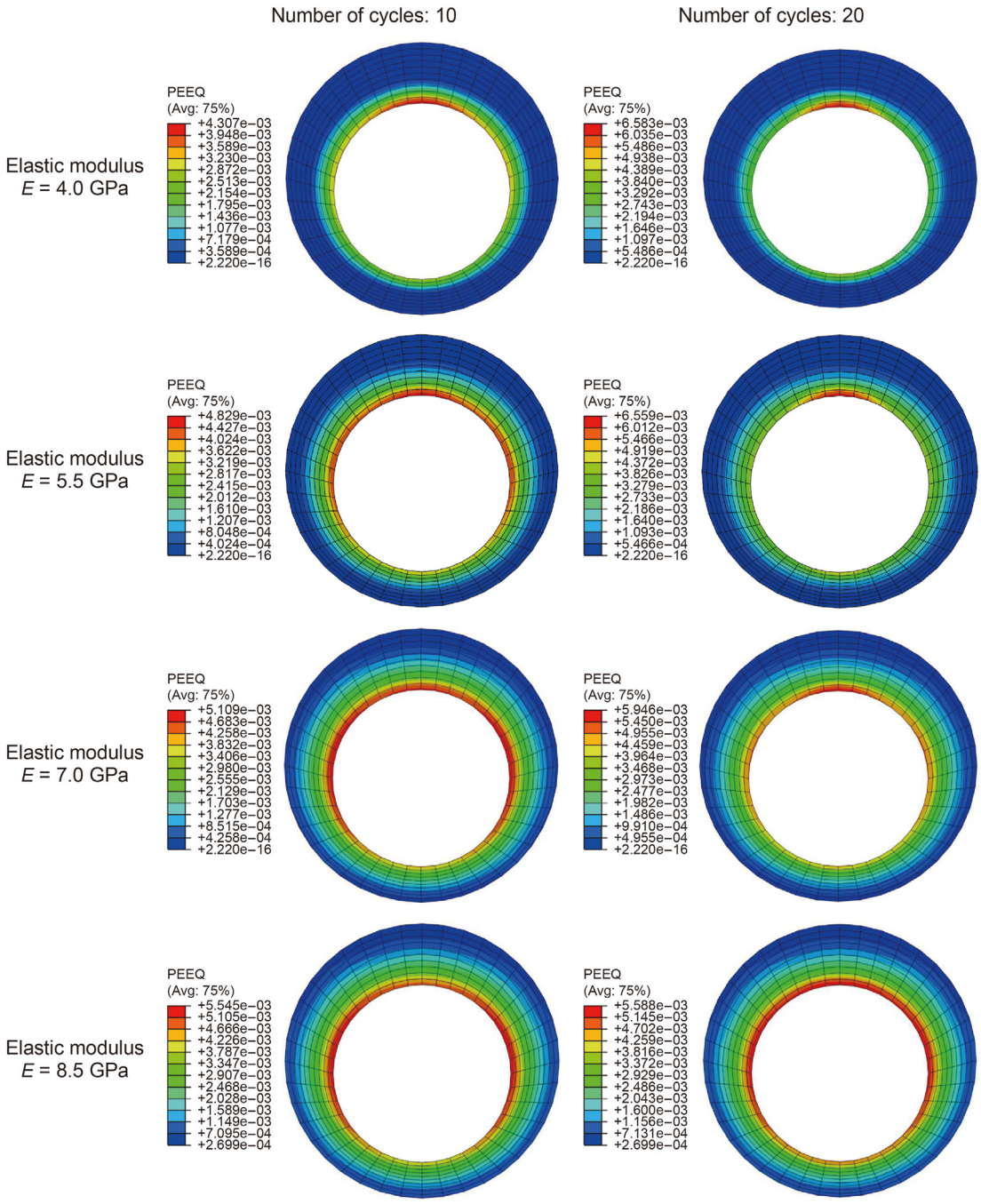

Fig. 19. Accumulated plastic deformations of cement sheaths under different elastic modulus conditions.

eccentric casing conditions or conduct corresponding numerical simulations and analyses. The eccentricity angle was 0° and the eccentricity distance was maintained at 10 mm in this study to change the elastic modulus of the cement sheath during the numerical simulation. The area with more significant cumulative plastic deformation continued to grow in the distribution area of the cumulative plastic deformation as the elastic modulus increased, as shown in Fig. 19.

The cumulative plasticity increased with continuous growth of the elastic modulus when the number of loading and unloading cycles was 10. Conversely, the cumulative plastic deformation decreased as the number of loading and unloading cycles increased to 20. This suggested that the cumulative deformation value was influenced by the elastic modulus and number of loading and unloading cycles. Therefore, it is necessary to simultaneously consider both factors when evaluating the sealing integrity of cement sheaths. The generation and development of the MA under different elastic moduli were calculated, as shown in Fig. 20.

The initial plastic deformation significantly decreased as the elastic modulus decreased. However, at the same time, a smaller elastic modulus corresponded to a more significant growth slope. This caused the cumulative plastic deformation to be influenced by the elastic modulus and number of loading and unloading cycles. A lower elastic modulus was beneficial for reducing the final cumulative plastic deformation when the number of loading and unloading cycles was low but exceeded a specific value.

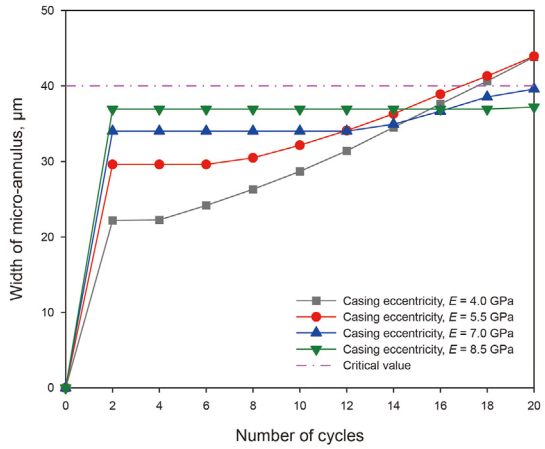

Fig. 20. Generation and development of MA under different elastic moduli.

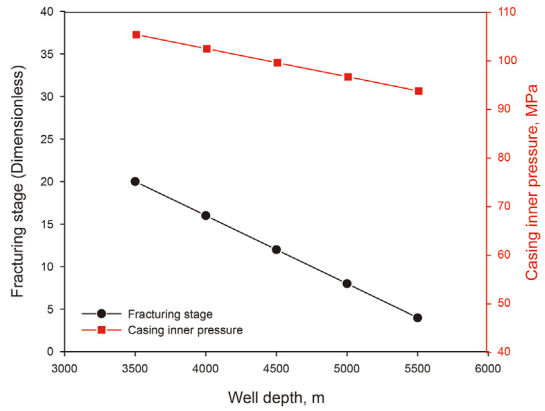

Fig. 21. Variations of fracturing stages and casing internal pressures with well depth.

4.3.4. Influence of well depth in the horizontal section

The frictional resistance of the entire horizontal section continued to increase as the well depth increased owing to the influence of the static fluid column pressure, wellhead pressure, and frictional resistance on the internal pressure of the casing. This caused a continuous reduction in the internal pressure of the casing, as shown in Fig. 21.

The eccentricity angle and distance were set to 0° and 15 mm, respectively. Simultaneously, the development law of cumulative plastic deformation was compared under the condition of casing centering, as shown in Fig. 22. The cumulative plastic deformation increased as the well depth decreased from the toe to heel end in the horizontal section. This was owing to the influence of the cyclic loading and unloading times and changes in the internal pressure of the casing. At the same position, the amount of cumulative plastic deformation for casing eccentricity was higher than that for casing centering. Additionally, casing eccentricity further increased the risk of cement sheath sealing integrity failure.

The change in the generation and development of the cement annulus in the horizontal section is shown in Fig. 23. The closer the heel, the greater the risk of sealing integrity failure owing to the high internal pressure of the casing and the frequent loading and unloading cycles.

There were 16 fracturing stages at a well depth of 4000 m. The width of the MA was approximately 28.9 μm when the casing was in the middle after 16 cycles of internal pressure loading and unloading in the casing. This was lower than the critical value of gas channeling for the width of the MA. However, the width of the MA reached 39.5 μm when there was eccentricity in the casing, approaching the critical value of gas channeling. In addition, the sealing integrity of the cement sheath in the current section did not fail for locations with well depths ranging from 3500 to 4000 m when the casing was centered. In contrast, the sealing integrity in this section had already failed when the casing was eccentric.

5. Engineering application cases

As previously mentioned, the results of this study can guide the selection of cement slurry types in horizontal sections. Therefore, an analysis was conducted at an engineering site based on the actual situation of the project.

A shale gas well in Luzhou, Sichuan Basin, China, was selected for analysis. The well had measured and acutal vertical depths of 5285 and 3654 mm, repsectively. The horizontal section was segmented into 20 equal subsections of 80 m. The wellbore was 215.9 mm in diameter. The production casing was made of P110 steel with a 139.7 mm outer diameter and thickness of 9.17 mm. Its elastic modulus and Poisson's ratio were 206 GPa and 0.3, respectively. The fracturing fluid density was 1.06 g/cm^3 and the treating pressure was 74 MPa. The displacement of the fracturing fluid was 18 m^3/min and the frictional resistance along the casing during the fracturing process was 0.008 MPa/m, as obtained from onsite engineering measurement data. The maximum and minimum horizontal principal stresses were 108 and 87 MPa, respectively, and the vertical principal stress was 98 MPa.

The distribution of the MA width along the horizontal section under the condition of casing centering is shown in Fig. 24. The width of the micro-annular gap in the horizontal section decreased as the well depth increased when the casing was in the center under the combined action of internal pressure and cyclic loading and unloading. The closer to the heel, the wider the width of the micro-ring gap and the greater the risk of cement-ring sealing integrity failure. However, even at the heel, the maximum width was only 32.1 μm, which was below the critical value of gas channeling.

The MA width along the horizontal section under the condition of casing eccentricity considering different elastic moduli is shown in Fig. 25.

The following observations were ascertained from the figure.

(a) The width of the micro-annular gap generated after the eccentricity of the casing was notably higher than that when the casing was centered. The width of the MA after the 20th fracturing stage reached 40.6 μm when the elastic modulus was 5.5 GPa. In addition, the width of the MA was 26.5% higher than that when the casing was centered under the same conditions.

(b) The micro-annular gap width was affected more intricately by various elastic moduli for the entire horizontal section because it was influenced by the internal casing pressure and loading and unloading cycle counts. A lower modulus of elasticity indicated a narrower width of the formed MA at the site close to the toe end. However, the closer the heel end, the greater the growth rate of the low elastic modulus cement sheath MA width. The more relative to the heel, the higher the elastic modulus and the lower the width of the resulting MA.

(c) The cement sheath with low and high elastic moduli formed an MA that was equal under cyclic loading and unloading when the fracturing stage was 16. However, the MA formed by the cement sheath with high elastic modulus was lower as the heel continued to approach. Based on this, cement slurry

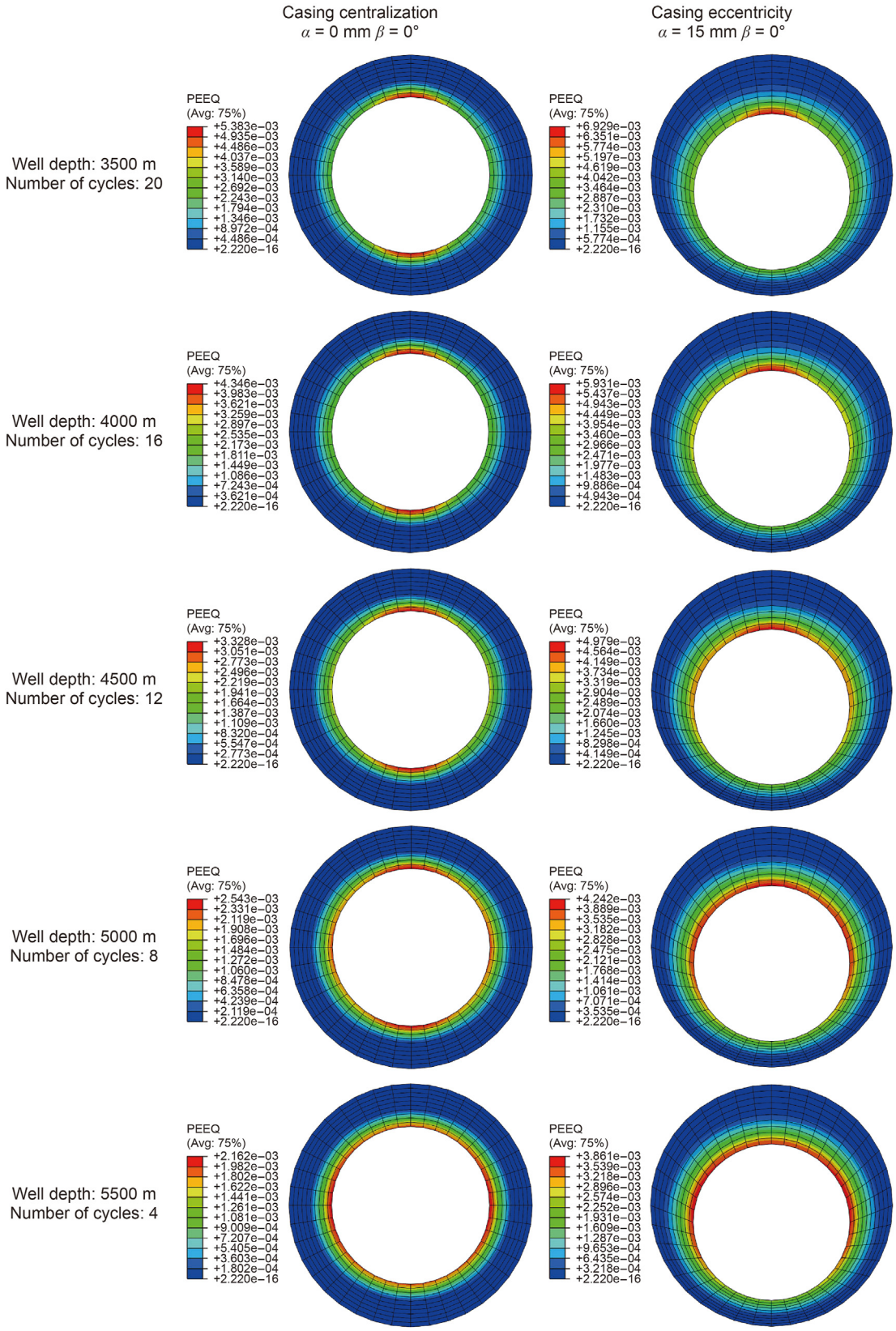

Fig. 22. Accumulated plastic deformations at different well depths.

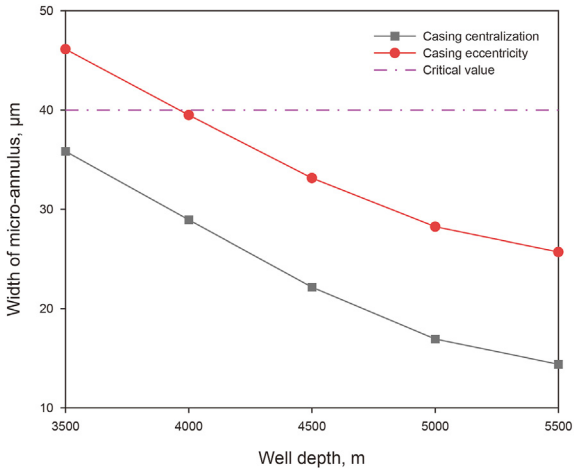

Fig. 23. Changes in the width of cement MA at different well depths.

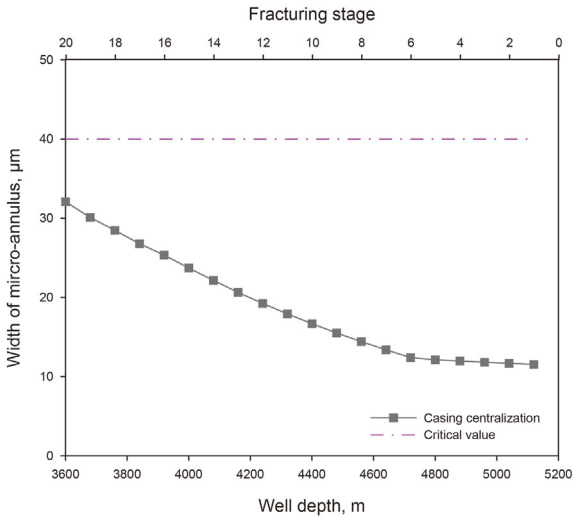

Fig. 24. MA width along the horizontal section under casing centering.

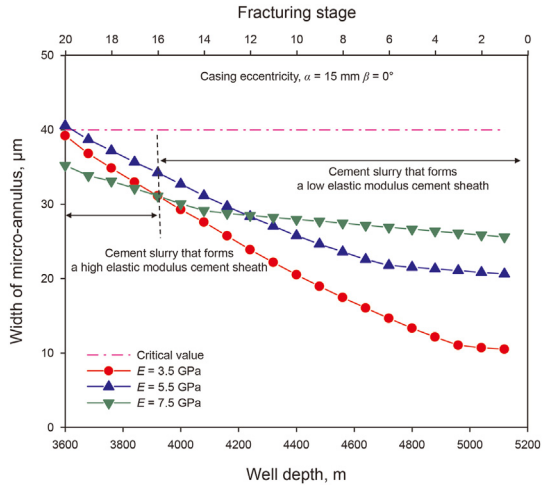

Fig. 25. MA width along the horizontal section under casing eccentricity.

with low elastic modulus should be used to form a cement sheath when the fracturing stage is from 1 to stage 16. Cement slurry that can form a high elastic modulus cement sheath can be applied after the 16th fracturing stage.

It can be seen from this that controlling the eccentricity of the casing in the horizontal section is of great significance for protecting the integrity of the cement sheath. Therefore, in the process of cementing operations, it is of great significance to design the position of the stabilizer reasonably or use the floating casing process to ensure that the casing is centered.

6. Conclusions

This study established a numerical model considering casing eccentricity, three-dimensional geo-stress, and cyclic loading and unloading that was used to analyze the law of cumulative plastic deformation and the emergence and development of micro-annulus. The conclusions are summarized as follows:

(1) A full-scale cement sheath integrity measurement device was used to measure the cumulative plastic deformation under the condition of casing centering. A numerical model for calculating the cumulative plastic deformation was established considering the casing eccentricity, three-dimensional geo-stress, and cyclic loading and unloading. The results of the numerical model calculations and experimental findings showed a relatively similar pattern, fully verifying the accuracy of the numerical simulation results.

(2) The eccentricity of the casing significantly increased the cumulative plastic deformation at the inner wall of the cement sheath, increasing the risk of sealing integrity failure. The cumulative plastic deformation at the inner wall of the cement sheath increased with a continuous increase of eccentricity when the eccentricity angle was 0°. The initial plastic deformation continuously increased as the eccentricity angle increased when the eccentricity was constant. However, the cumulative plastic deformation constantly decreased after a specific number of loading and unloading cycles.

(3) The distribution of the MA on the horizontal section continuously increased from the toe to the heel under the combined influence of internal pressure, internal friction, and cyclic loading and unloading times. The width of the MA near the toe end decreased as the elastic modulus of the cement sheath decreased. However, the width of the MA near the heel end increased.

(4) The cement sheaths with low and high elastic moduli formed an equal MA under cyclic loading and unloading when the fracturing stage reached a specific value. Cement slurries with low and high elastic moduli can be used to form cement sheaths when the fracturing stages are below or above specific values, respectively.

CRediT authorship contribution statement

Yan Xi: Writing – original draft, Conceptualization. **Yu Yao:** Formal analysis. **Xue-Li Guo:** Resources. **Jun Li:** Writing – review & editing. **Yu-Dong Tian:** Resources. **Gong-Hui Liu:** Supervision.

Declaration of competing interest

The authors declare no conflict of interest.

Acknowledgments

This study was financially supported by the National Natural Science Foundation of China (Grant No. 52374001, No. 52004013).

References

Andrade, J.D., Sangesland, S., Skorpa, R., Todorovic, J., Vrålstad, T., 2016. Experimental laboratory setup for visualization and quantification of cement-sheath integrity. SPE Drill. Eng. 31 (4), 317–326. https://doi.org/10.2118/173871-PA.

Arjomand, E., Bennett, T., Nguyen, G.D., 2018. Evaluation of cement sheath integrity subject to enhanced pressure. J. Petrol. Sci. Eng. 170, 1–13. https://doi.org/10.1016/j.petrol.2018.06.013.

Benzeggagh, M.L., Kenane, M., 1996. Measurement of mixed-mode delamination fracture toughness of unidirectional glass/epoxy composites with mixedmode bending apparatus. Compos. Sci. Technol. 56, 439–449. https://doi.org/10.1016/0266-3538(96)00005-X.

Bu, Y.H., Ma, R., Guo, S.L., Du, J.P., Liu, H.J., Cao, X.C., 2020. A theoretical evaluation method for mechanical sealing integrity of cementing sheath. Appl. Math. Model. 84, 571–589. https://doi.org/10.1016/j.apm.2020.03.001.

Carter, L.G., Evans, G.W., 1964. A study of cement-pipe bonding. J. Petrol. Technol. 16 (2), 157–160. https://doi.org/10.2118/764-PA.

Chen, S., Jin, J.Z., Shen, J.Y., Guo, X.L., Wang, L.L., 2023. Monitoring evolution of temperature and strain in cement sheath using embedded optical fiber bragg gratings. SPE J. 28 (1), 19–31. https://doi.org/10.2118/212264-PA.

Chu, W., Shen, J.Y., Yang, Y.F., Li, Y., 2015. Calculation of micro-annulus size in casing-cement sheath-formation system under continuous internal casing pressure. Petrol. Explor. Dev. 42 (3), 414–421. https://doi.org/10.1016/S1876-3804(15)30033-1.

Deng, K.H., Xie, P.F., Yuan, Y., Zeng, D.Z., Li, Q., Lin, Y.H., 2021. Study on the effect of interface failure between casing and cement sheath on casing stress under non-uniform in-situ stress. Appl. Math. Model. 91, 632–652. https://doi.org/10.1016/j.apm.2020.10.007.

Deng, K.H., Zhou, N.T., Lin, Y.H., Wu, Y.X., Chen, J., Shu, C., Xie, P.F., 2023. Failure mechanism and influencing factors of cement sheath integrity under alternating pressure. Petrol. Sci. 20 (4), 2413–2427. https://doi.org/10.1016/j.petsci.2023.03.004.

Feng, Y.C., Li, X.R., Gray, K.E., 2017. Development of a 3D numerical model for quantifying fluid-driven interface debonding of an injector well. Int. J. Greenh. Gas Control 62, 76–90. https://doi.org/10.1016/j.ijggc.2017.04.008.

Goodwin, K.J., Crook, R.J., 1992. Cement sheath stress failure. SPE Drill. Eng. 7 (4), 291–296. https://doi.org/10.2118/20453-PA.

Gu, C.W., Li, X.R., Feng, Y.C., Deng, J.G., Gray, K., 2022. Numerical investigation of cement interface debonding in deviated shale gas wells considering casing eccentricity and residual drilling fluid. Int. J. Rock Mech. Min. Sci. 158, 105197. https://doi.org/10.1016/j.ijrmms.2022.105197.

Guo, B.Y., Shan, L.Q., Jiang, S.X., Li, G., Lee, J., 2018. The maximum permissible fracturing pressure in shale gas wells for wellbore cement sheath integrity. J. Nat. Gas Sci. Eng. 56, 324–332. https://doi.org/10.1016/j.jngse.2018.06.012.

Han, X., Feng, F.P., Zhang, X.C., Cao, J., Zhang, J., Suo, Y., Yan, Y., Yan, M.S., 2023. An unequal fracturing stage spacing optimization model for hydraulic fracturing that considers cementing interface integrity. Petrol. Sci. 20 (4), 2165–2186. https://doi.org/10.1016/j.petsci.2023.05.010.

Huang, Y., Chen, H.D., Zheng, H.P., Liu, Y., Zheng, H.D., 2022. Influence of casing eccentricity on mechanical integrity of cement sheath in fractured wells. China Offshore Oil Gas 34 (6), 135–141. https://doi.org/10.11935/j.issn.1673-1506.2022.06.014 (in Chinese).

Jafariesfad, N., Sangesland, N., Gawel, K., Torsæter, M., 2020. New materials and technologies for life-lasting Cement Sheath: a review of recent Advances. SPE Drill. Complet. 35 (2), 262–278. https://doi.org/10.2118/199885-PA.

Li, J., Xi, Y., Tao, Q., Li, Y.M., Qu, G.H., 2020. Experimental investigation and numerical simulation of the emergence and development of micro-annulus in shale gas wells subjected to multistage fracturing. J. Nat. Gas Sci. Eng. 78, 103314. https://doi.org/10.1016/j.jngse.2020.103314.

Li, X.R., Gu, C.W., Ding, Z.C., Feng, Y.C., 2023. THM coupled analysis of cement sheath integrity considering well loading history. Petrol. Sci. 20 (1), 447–459. https://doi.org/10.1016/j.petsci.2022.09.001.

Lian, W., Li, J., Tao, Q., Du, J.L., Wang, L., Xi, Y., 2020. Formation mechanism of continuous gas leakage paths in cement sheath during hydraulic fracturing. Energy Sci. Eng. 7, 2527–2547. https://doi.org/10.1002/ese3.684.

Liu, K., Ding, S.D., Zhou, S.M., Tao, Q., Zhang, L.H., Liu, R.G., Gao, D.L., 2021. Study on preapplied annulus backpressure increasing the sealing ability of cement sheath in shale gas wells. SPE J. 26 (6), 3544–3560. https://doi.org/10.2118/205360-PA.

Liu, R.G., Zhang, L.H., Tao, Q., Zhou, S.M., Ding, S.D., 2016. Experimental study on airtightness of cement sheath under alternating stress. Drill. Fluid Complet. Fluid 33 (4), 74–78. https://doi.org/10.3696/j.issn.1001-5620.2016.04.015 (in Chinese).

Meng, M., Frash, L., Carey, J.W., Niu, Z.H., Zhang, W.C., Guy, N., Lei, Z., Li, W.F., Nathan, W., 2021. Predicting cement-sheath integrity with consideration of initial state of stress and thermoporoelastic effects. SPE J. 26 (6), 3505–3528. https://doi.org/10.2118/205344-PA.

Obando Palacio, G., Gardner, D., Delabroy, L., Amit, G., 2020. An evaluation of the cement sheath quality of casing sections recovered during a well abandonment operation. The IADC/SPE International Drilling Conference and Exhibition, Galveston, Texas. https://doi.org/10.2118/199609-MS.

Shadravan, A., Schubert, J., Amani, M., Teodoriu, C., 2015. Using fatigue-failure envelope for cement-sheath-integrity evaluation. SPE Drill. Complet. 30 (1), 68–75. https://doi.org/10.2118/168321-PA.

Wang, W., Dahi Taleghani, A., 2014. Three-dimensional analysis of cement sheath integrity around wellbores. J. Petrol. Sci. Eng. 121, 38–51. https://doi.org/10.1016/j.petrol.2014.05.024.

Wang, W., Dahi Taleghani, A., 2017. Impact of hydraulic fracturing on cement sheath integrity; A modelling approach. J. Nat. Gas Sci. Eng. 44, 265–277. https://doi.org/10.1016/j.jngse.2017.03.036.

Wang, Y.B., Liu, K., Gao, D.L., 2021. Investigation of the interface cracks on the cement sheath stress in shale gas wells during hydraulic fracturing. J. Petrol. Sci. Eng. 205, 108981. https://doi.org/10.1016/j.petrol.2021.108981.

Wei, S.M., Kuru, E., Jin, Y., Yang, X.X., 2022. Numerical investigation of the factors affecting the cement sheath integrity in hydraulically fractured wells. J. Petrol. Sci. Eng. 215, 110582. https://doi.org/10.1016/j.petrol.2022.110582.

Xi, Y., Li, J., Liu, G.H., Tao, Q., Lian, W., 2018. A new numerical investigation of cement sheath integrity during multistage hydraulic fracturing shale gas wells. J. Nat. Gas Sci. Eng. 49, 331–341. https://doi.org/10.1016/j.jngse.2017.11.027.

Xi, Y., Li, J., Tao, Q., Guo, B.Y., Liu, G.H., 2020. Experimental and numerical investigations of accumulated plastic deformation in cement sheath during multistage fracturing in shale gas wells. J. Petrol. Sci. Eng. 187, 106790. https://doi.org/10.1016/j.petrol.2019.106790.

Xi, Y., Lian, W., Fan, L.F., Tao, Q., Guo, X.L., 2021. Research and engineering application of pre-stressed cementing technology for preventing micro-annulus caused by cyclic loading-unloading in deep shale gas horizontal wells. J. Petrol. Sci. Eng. 200, 108359. https://doi.org/10.1016/j.petrol.2021.108359.

Xi, Y., Jin, J.Z., Fan, L.F., Guo, X.L., Shen, J.Y., Li, J., 2022. Research on the establishment of gas channeling barrier for preventing SCP caused by cyclic loading-unloading in shale gas horizontal wells. J. Petrol. Sci. Eng. 208, 109640. https://doi.org/10.1016/j.petrol.2021.109640.

Xu, X.N., Zhao, B.Z., Huang, H., Wei, R.H., Cao, G.F., Yang, H., Zhou, P.G., 2022. Study on cement sheath failure mechanism for stimulated reservoir volume in shale oil horizontal wells. China Petrol. Machin. 50 (11), 73–80. https://doi.org/10.16082/j.cnki.issn.1001-4578.2022.11.011.

Yan, W., Wei, H.G., Muchiri, N.D., Li, F.L., Zhang, J.R., Xu, Z.X., 2023. Degradation of chemical and mechanical properties of cements with different formulations in CO_2-containing HTHP downhole environment. Petrol. Sci. 20 (2), 1119–1128. https://doi.org/10.1016/j.petsci.2023.03.012.

Yan, Y., Guan, Z.H., Zhang, B., Chen, W.Q., 2021. Numerical investigation of debonding extent development of cementing interfaces during hydraulic fracturing through perforation cluster. J. Petrol. Sci. Eng. 197, 107970. https://doi.org/10.1016/j.petrol.2020.107970.

Zeng, B., Wang, D., Song, Y., Lian, W., Li, J., 2022. Integrity analysis of cement sheath in annulus of vertical section during hydraulic fracturing. China Petrol. Machin. 50 (8), 89–95. https://doi.org/10.16082/j.cnki.issn.1001-4578.2022.08.013.

Zeng, Y.J., Liu, R.G., Li, X.J., Zhou, S.M., Tao, Q., Lu, P.Q., 2019. Cement sheath sealing integrity evaluation under cyclic loading using largescale sealing evaluation equipment for complex subsurface settings. J. Petrol. Sci. Eng. 176, 811–820. https://doi.org/10.1016/j.petrol.2019.02.014.